SCIENCE CHINA Materials ARTICLES

mater.scichina.com link.springer.com

Published online 28 June 2020 | https://doi.org/10.1007/s40843-020-1370-x
Sci China Mater 2021, 64(1): 85–95

Enhancing sodium-ion storage performance of MoO_2/N-doped carbon through interfacial Mo–N–C bond

Bin Huang[1], Shuang Liu[1], Xu Zhao[2*], Yanwei Li[1], Jianwen Yang[1], Quanqi Chen[1], Shunhua Xiao[1], Wenhua Zhang[2], Hong-En Wang[4*] and Guozhong Cao[3*]

ABSTRACT **Na-ion batteries (SIBs) have attracted considerable attention as promising alternatives to commercial Li-ion batteries (LIBs) due to comparable redox potential, and natural abundance of Na. However, it remains challenging to explore suitable anodes for SIBs. Herein, a MoO_2/N-doped carbon (MoO_2/N-C) composite composed of MoO_2 nanocrystals embedded within carbon matrix with a Mo–N–C chemical bond is prepared by a simple yet effective carbonization-induced topochemical transformation route. Na-ion half-cells using MoO_2/N-C exhibit excellent cycling stability over 5000 cycles at 5 A g^{-1} and superior rate capability. Physicochemical characterizations and first-principles density functional theory (DFT) simulations reveal that the formation of chemical bond at the interface between MoO_2 and N-doped carbon plays an important role in the excellent charge storage properties of MoO_2/N-C. More importantly, the interfacial coupling can efficiently promote interface charge transfer. Benefiting from this, Na-ion capacitors (SICs) constructed with the MoO_2/N-C anode and activated carbon cathode can deliver an impressive energy density of 15 W h kg^{-1} at a power density of 1760 W kg^{-1}, together with a capacitance retention of 92.4% over 1000 cycles at 10 A g^{-1}. The proposed strategy in this paper based on interfacial chemical bond may hold promises for the design of high-performance electrodes for energy storage devices.**

Keywords: topochemical transformation, Mo–N chemical bond, Na-ion batteries, Na-ion capacitor, density functional theory simulations

INTRODUCTION

Rechargeable lithium ion batteries (LIBs) have attracted considerable attention among various clean energy technologies due to their portability and high energy-conversion efficiencies [1]. However, the rare and high cost resources of Li stimulate the development of novel energy storage techniques. Among them, Na-ion batteries (SIBs) are triggering tremendous research interests as alternative candidates to current LIBs due to low cost and resource abundance of sodium [2,3]. Although the physicochemical similarity of Na^+ to that of Li^+ might be predicted, it remains challenging and unsuitable to directly transplant anode materials in LIBs to store Na^+ mainly due to the larger ionic radius relative to Li^+ [4]. Therefore, to exploit suitable host materials for Na-ion storage has been a challenge so far. The electrochemical performances of carbon-based anode in SIBs have been enhanced through interlayer engineering and heteroatom doping strategies [5], but the limited capacities still hinder their practical applications [6]. Transition metal oxides (TMOs) can possess higher theoretical capacities compared with carbonaceous materials, showing great potential as novel anode materials for SIBs [7–9]. Nevertheless, the further practical operation of TMOs in SIB and potassium ion battery (PIB) suffers from low reversible capacity and rapid capacity fade during cycling. Its low reversible capacity is due to the low conductivity of a traditional TMO and the slow reaction kinetics for Na^+ insertion/extraction. Among various TMOs, molybdenum dioxide (MoO_2) with relatively high electronic conductivity has been considered as an alternative electrode material for Li/Na-ion storage [10–12]. However, the electrochemical performance of MoO_2 in SIBs is still restricted by the large volume fluctuation during the so-

[1] Guangxi Key Laboratory of Electrochemical and Magneto-chemical Functional Materials, College of Chemistry and Bioengineering, Guilin University of Technology, Guilin 541004, China
[2] Institute of Chemical Materials, China Academy of Engineering Physics, Mianyang 621900, China
[3] Department of Materials Science and Engineering, University of Washington, Seattle, WA 98195, USA
[4] College of Physics and Electronics Information, Yunnan Normal University, Kunming 650500, China
* Corresponding authors (emails: xuzhao@caep.cn (Zhao X); hongen.wang@outlook.com (Wang HE); gzcao@u.washington.edu (Cao G))

diation/de-sodiation process. One effective strategy for abating the volume change of MoO_2 is confining it within some elastic substrate such as carbon materials. Recently, Hao *et al.* [13] improved the cycling stability of MoO_2 anode through coupling MoO_3 and reduced graphene oxide (rGO) to construct MoO_3/MoO_2-rGO ternary heterostructure. More efforts are desired to further construct the chemical combination between MoO_2 and carbon for fast charge transfer kinetics that dictates their usage in advanced batteries.

Here we implement the controllable synthesis of a MoO_2/N-doped carbon composite (denoted as MoO_2/N-C) for advanced SIBs through a topotactical process [14] of annealing the Mo-polydopamine (Mo-PDA) complex. *In-situ* X-ray photoelectron spectroscopy (*in-situ* XPS) revealed a step-by-step dissociation of Mo-PDA from the amorphous state to crystalline MoO_2/N-doped carbon. During such a process, the Mo–N–C chemical bond could be achieved under a desired temperature (i.e., 500°C) and then removed at a higher temperature (i.e., 700°C). The resulting composite has several structural advantages for SIB: (1) metallic MoO_2 and high-conductive N-carbon matrix could effectively promote the electron transfer. (2) During the annealing process, the Mo–N–C chemical bond formed at the interface between MoO_2 and N-doped carbon could possibly be attributed to the evolution of Mo–N–C functional groups in Mo-PDA chelate. The role of the interfacial chemical bond was revealed *via* density functional theory (DFT) simulations, which was shown to promote charge accumulations at the interface between MoO_2 and N-doped carbon. (3) Tunable pores located between two adjacent MoO_2 crystals could be achieved by changing the annealing temperature, which featured additional sites for Na-ion permeation with fast ionic diffusion capability. Consequently, the MoO_2/N-C anode with interfacial Mo–N–C bond manifested excellent electrochemical performance in terms of high capacity, long cycling stability and superior rate capability, demonstrating great potential for application in large-scale energy storage devices. The schematics of synthesis and kinetic promotion are shown in Fig. 1.

EXPERIMENTAL SECTION

All the chemicals were purchased from Sigma-Aldrich and used directly.

The preparation of MoO_2/N-C

Four gram of $(NH_4)_6Mo_7O_{24}{\cdot}4H_2O$ (99%) and 1 g of dopamine hydrochloride was firstly dissolved in 400 mL deionized (DI) water under stirring for 20 min (denoted as solution A). Then 800 mL of pure ethanol were quickly poured into solution A, forming a dark orange solution (named as solution B). After stirring for another 20 min, 6 mL $NH_3{\cdot}H_2O$ was quickly injected into solution B. After being continuously stirred for 2 h at room temperature, the orange precipitate was harvested by centrifugation,

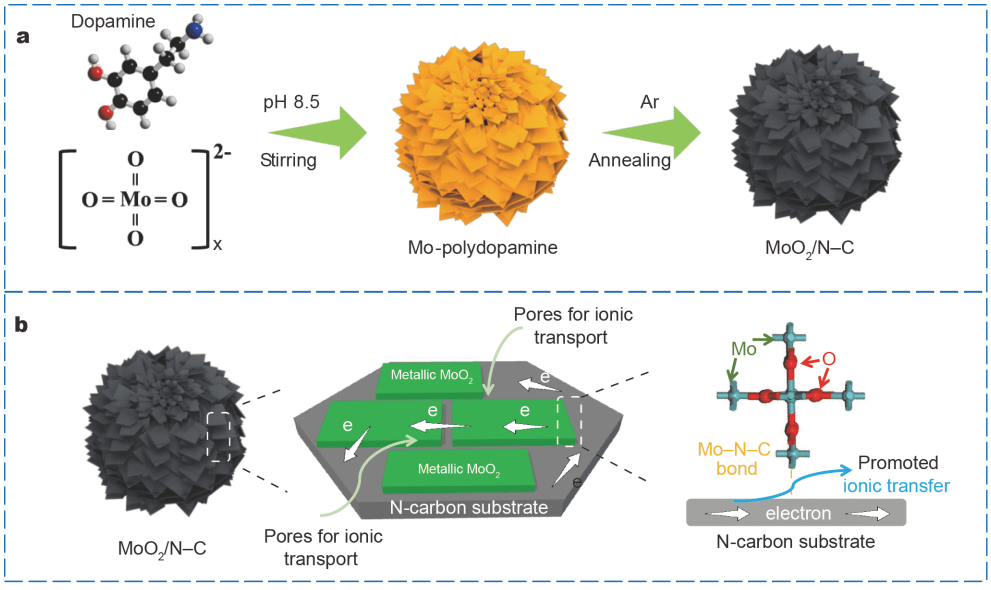

Figure 1 (a) The synthetic route from Mo-polydopamine precursor to the MoO_2/N-C product. (b) Illustration of electron and ionic transport properties in MoO_2/N-C, in which MoO_2 are bridged with N-carbon *via* Mo–N–C chemical bond.

washed with ethanol and DI water for several rounds and dried at 70°C overnight to get Mo-PDA precursors. Then the final products were obtained after annealing Mo-PDA at 350, 500 and 700°C for 2 h with a ramping rate of 2°C min^{-1}.

Structural measurements

The crystal structure was characterized by an X-ray diffraction (XRD) instrument (PANalytical X'Pert Pro X-ray diffractometer). The morphology and microstructure were characterized by scanning electron microscope (SEM, FEI Helios Nanolab 600i) and transmission electron microscope (TEM, FEI Tecnai G2 F-20, 200 kV). The high angle annular dark-field scanning transmission electron microscopy (HAADF-STEM) images and corresponding energy dispersive X-ray spectroscopy (EDS) mappings were conducted using an FEI-Talos TEM instrument at the same working voltage (200 kV). The surface elemental composition and chemical state were analyzed by XPS (Thermo Fisher Scientific ESCALAB 250-Xi) with Al Kα radiation. *In-situ* XPS patterns were conducted using the same instrument with a ramping rate of 5°C min^{-1} from room temperature to 700°C. The specific surface areas and pore volume of the as-synthesized materials were measured using Brunauer-Emmett-Teller (BET) method at liquid-nitrogen condition in Quantachrome NOVA 4200e instrument. Thermogravimetric analysis (TGA) was conducted on a Netzsch TG 209-F3 in compressed air with temperature ramping rate of 10 °C min^{-1}.

Assembly of Na-ion half-cell and Na-ion capacitors

Active materials (MoO_2/N-C), KJ-black carbon and sodium carboxymethyl cellulose (CMC) binder were mixed in a weight ratio of 8:1:1 for 1 h. Then a certain amount of DI water was added to form a slurry, which was pasted on a piece of Cu using a doctor-blade. The as-obtained electrode was pre-dried in a 40°C oven for 1 h. After that, the electrode was cut into several circles with a diameter of 10 mm. The average mass loading of electrode in this paper was about 1.3–1.6 mg cm^{-2}. Finally, the circles were dried under vacuum at 110°C for 8 h before being transferred into Ar-filled glovebox. For Na-ion half-cells, the electrolyte was 1 mol L^{-1} $NaClO_4$ in ethylene carbonate/diethyl carbonate (EC/DEC) (1:1 vol%) with 5 vol% flouroethylene carbonate (FEC) addictive. Glass-fiber (Type-D) and fresh-made sodium foils were selected as the separator and counter electrode, respectively. For sodium ion capacitors (SICs), sodiated MoO_2/N-C and commercial activated carbon (purchased from XF-Nano) were chosen as anodes and cathodes without changing the electrolyte components and separator. The volume of electrolyte in the SIB and SIC was fixed to 120 μL.

Simulation detail

Spin-polarized first-principles DFT calculations were carried out using CASTEP module in Materials Studio software. The exchange and correlation energies were described using OTFG ultrasoft pseudopotential (USPP) and Perdew-Burke-Ernzerhof (PBE) functional within the generalized gradient approximation (GGA). The electron-ion interactions were scheduled within a plane-wave basis set with an energy cutoff of 400 eV for surface and 600 eV for band structure calculations, respectively. The effects of coupling with N-doped carbon on the electrochemical properties of MoO_2 were investigated by using a graphene sheet doped with N atoms for simplicity. The MoO_2 was modelled by a Mo-O molecular unit for simplicity. To simulate the interactions between MoO_2 and N-doped carbon, a surface slab containing (6×6) graphene single sheet with a vacuum layer of 15 Å was used to avoid the unwanted interactions between neighboring mirrors along *z*-direction. The convergence criteria of the total energy with respect to the k-points sampling and the energy-cutoff were carefully examined, using 1×1×1 Monkhorst-Pack k-points grid for the surface slabs and 6×6×6 k-mesh for band structure calculations together with a Hubbard potential of U=3.25 eV (DFT+U method). Ionic relaxations were performed using a conjugate gradient (CG) algorithm until the net force on all individual atoms was less than 0.05 eV $Å^{-1}$, the self-consistent field (SCF) tolerance was set to 2.0×10^{-6} eV $atom^{-1}$ for geometry optimization. The adsorption energy (E_{ads}) for Na, VO, V or Na_2S on N-doped (or pristine) graphene surface was determined using $<E_{ads}=E_{total}-E_{surf}-E_{mol}>$, where E_{total} is the total energy of the system containing the surface with a adsorbed molecule (or atom/ion), E_{surf} is the energy of the clean surface, E_{mol} is the energy of a free molecule or atom/ion in vacuum. During E_{ads} calculations, van der Waals interactions were included.

RESULTS AND DISCUSSION

The synthesis procedure of the MoO_2/N-C composite is demonstrated and illustrated in the experimental section and Fig. 1. Polymolybdic-acid-anions (MoO_x^{n-}) first chelated with dopamine molecules under weak alkaline condition (pH 8.5) [15], formed a Mo-polydopamine complex (Fig. S1) and then transformed to MoO_2/N-C after annealing in Ar. The annealing process was opti-

mized by changing the annealing temperature (350, 500 and 700°C) selected mainly based on the TGA results (Fig. S2) measured in N_2. The corresponding samples are referred as MoO_2/N-C (350°C), MoO_2/N-C (500°C) and MoO_2/N-C (700°C), respectively, for clarity.

Fig. 2a shows the XRD patterns of MoO_2/N-C (500°C) and MoO_2/N-C (700°C), resembling a crystal structure of MoO_2 (JCPDS Card No. 65-1273) with space group of *C*2/*m*. The intensities of the diffraction peaks become stronger as the annealing temperature increases. Instead, there is no obvious diffraction peaks for MoO_2 annealed at a relatively low annealing temperature (350°C, Fig. S3a), indicating that the MoO_2/N-C (350°C) is amorphous or not well crystallized [16]. No diffraction peaks assigned to carbon can be observed in the MoO_2/N-C obtained at various temperatures, suggesting the amorphous nature of the carbon. Raman spectra of the as-prepared samples (Fig. S3b) were further measured, verifying the existence of two peaks at ~1435 and ~1580 cm^{-1} that can be assigned to the D-band and G-band of carbon, respectively. It is deduced that polydopamine has been transformed into amorphous carbon with ample defects during the annealing in Ar. The carbon content of the MoO_2/N-C (500°C) sample could be examined using TGA in air and the results are presented in Fig. S3c. From the TGA curves, initial weight loss was observed below 100°C, which could be attributed to the loss of adsorbed water and residual small organic molecules. A significant weight loss occurred in the following stage is due to the combustion of carbon. According to the possible reaction ($2MoO_2+O_2 \rightarrow 2MoO_3$), MoO_2 in the as-prepared complex can be oxidized to MoO_3 in air. Therefore, the mass content of MoO_2 could be determined to be about 49%.

Fig. 2b, c show the *in-situ* XPS data to distinguish the element compositions and electronic states of the elements existing in the MoO_2/N-carbon composite surface. The shoulder peak assigned to the chelate species of Mo-PDA complex [17] at around 225–226 eV decreases with the increase of temperature, while the asymmetric peaks at 229–232 eV keep their positions, indicating the phase transition processes of Mo-PDA complex to MoO_2. The high-resolution Mo 3d bands are displayed in Fig. 2d. Apart from Mo^{4+} in MoO_2 with binding energies (BEs) at 228.9 and 232 eV [18], it should be noted that an obvious Mo–N bond is shown in the MoO_2/N-C (500°C) sample, implying a strong electron interaction between MoO_2 and N-carbon. In contrast, the peak assigned to Mo–N bond disappears when the temperature increases to 700°C, indicating the interfacial chemical bond would maintain at

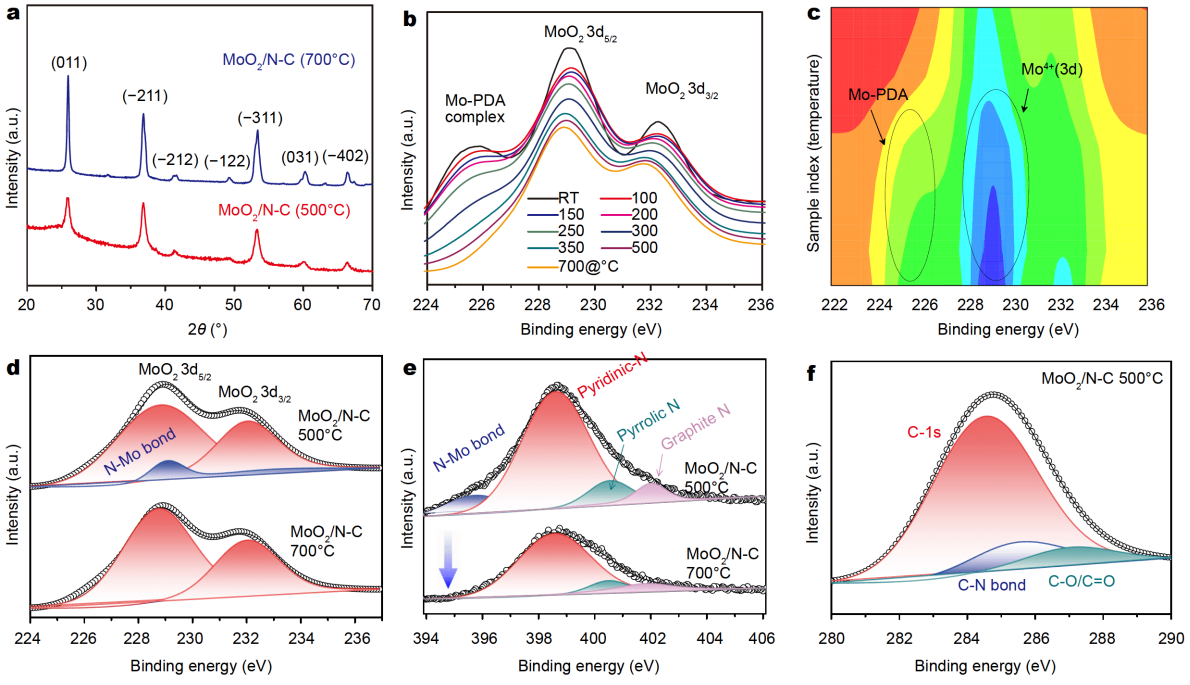

Figure 2 (a) XRD patterns of the MoO_2/N-C samples obtained at 500 and 700°C. (b, c) *In-situ* XPS results of Mo 3d during the heating processes at various temperatures, examining the topochemical phase transition of Mo-PDA complex to MoO_2. (d) The high-resolution Mo 3d band, (e) N 1s band and (f) C 1s band of MoO_2/N-C.

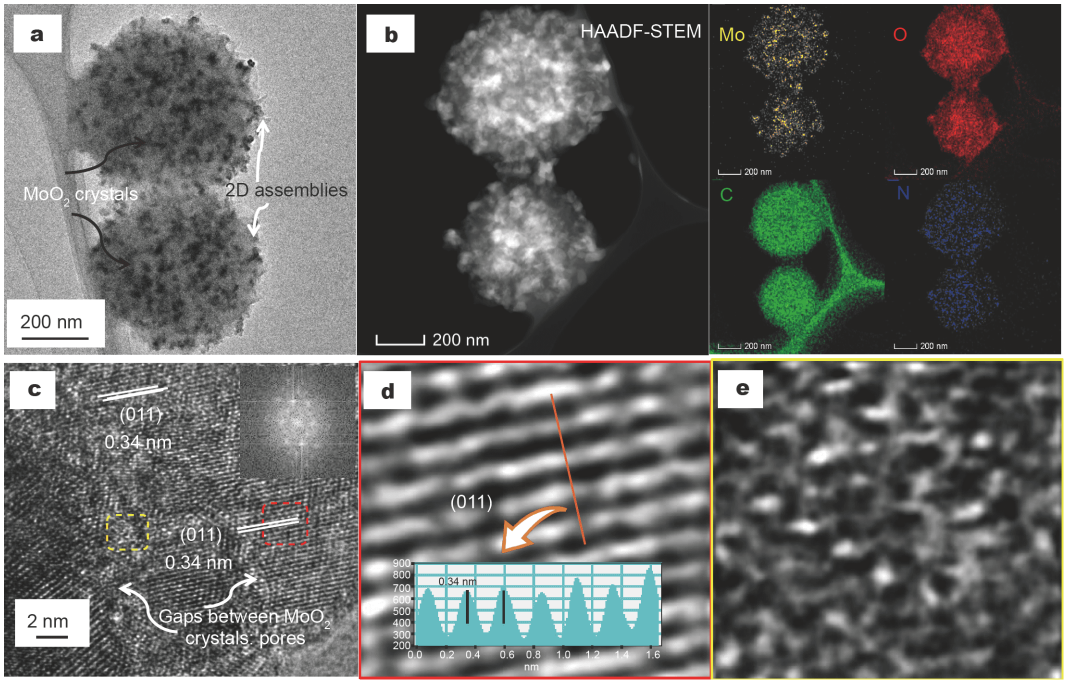

Figure 3 (a) TEM image of MoO_2/N-C (500°C). (b) HAADF-STEM image and corresponding elemental mapping of Mo, O, C and N. (c) HRTEM image of MoO_2/N-C (500°C), in which the inset shows the electron diffraction (ED) pattern. IFFT patterns of (d) red region and (e) yellow region in (c) and inset of (d) show the linear profile of the (011) facet.

500°C whereas the MoO_2 might physically contact with the carbon matrix after being calcined at 700°C. The N 1s spectra were further examined and shown in Fig. 2e. N 1s of the MoO_2/N-C (500°C) sample can be deconvoluted into five peaks at 396.1, 398.2, 400.7 and 402.4 eV, which are ascribed to N–Mo bond [19], pyridinic-N [20], pyrrolic-N [21] and graphite-N [22], respectively. The Mo–N bond disappears in MoO_2/N-C (700°C), which further indicates a physical contact between MoO_2 and the N-carbon matrix. The total nitrogen content in MoO_2/N-C decreases from 12.6% (500°C) to 7.4% (700°C), which may result from the nitrogen species wastage [23]. Notably, the dominated existence of pyridinic-N in both MoO_2/N-C (500°C) and MoO_2/N-C (700°C) could significantly boost the electrical transport in the carbon matrix by the donation of the lone-pair electrons from N species to the graphitic carbon matrix [20]. In addition, the C 1s signal (Fig. 2f) can be separately assigned to C–C bonding (284.8 eV) and C–O/C=O (287.2 eV) bonding. The formation of C–N at 285.9 eV suggests the nitrogen may act as a bridge at the interface between MoO_2 and carbon substrate, ensuring a strong electronic coupling in the whole materials. From the XPS results, the formation of Mo–N bond at the interface of N-carbon and MoO_2 can be confirmed, which may significantly reinforce the structural integrity and facilitate the charge transfer at the interface between MoO_2 and carbon during the electrochemical redox process [24].

The morphologies of the as-prepared MoO_2/N-C series were examined by scanning electron microscopy (SEM), which reveals that the MoO_2 hybrids possess a hierarchically spherical framework with a diameter of 400–500 nm (Fig. S4). The two-dimensional (2D) building blocks may exhibit large surface area for enlarged electrolyte contact [25]. Detailed microstructures were further confirmed *via* transmission electron microscopy (TEM) and high-resolution TEM (HRTEM) images. The TEM image of MoO_2/N-C (500°C) presents a hierarchical sphere with wrinkled 2D assemblies as crust and embedded MoO_2 crystals in the carbon matrix (Fig. 3a). In comparison, the microstructures of other two samples are slightly different (Fig. S5). Although 2D carbon substrates can be observed, there is a dense core when MoO_2/N-C (350°C) is observed, which may be caused by the different crystallinities as examined from the XRD patterns in Fig. S3a. The HAADF-STEM image of MoO_2/N-C (500°C) in Fig. 3b shows uniform bright white dots, which further confirms the existence of MoO_2 nanocrystals and carbon substrates. EDS collected from the whole area of Fig. 3b identifies the elemental signals, and

the corresponding elemental mapping shows homogeneously elemental distributions of Mo, O, C and N. The HRTEM image of MoO_2/N-C (500°C) (Fig. 3c) reveals that the lattice spacing is 0.34 nm, which corresponds to the (011) facet of MoO_2 [26]. Besides, some mesopores between the adjacent MoO_2 crystals could be observed, which could act as the extra pathway for ionic transportation. However, that kind of gap (pores) could not be seen in the MoO_2/N-C (700°C) sample as shown in the HRTEM (Fig. S6), implying a relatively small specific surface area. Specific surface areas of the three samples were estimated from N_2 adsorption/desorption isotherms (Fig. S7). The small hysteresis of P/P_0 range of 0.6–0.9 indicates the presence of mesopores in the MoO_2/N-C (500°C) sample. The specific surface areas of MoO_2/N-C (350°C), MoO_2/N-C (500°C) and MoO_2/N-C (700°C) are 42.21, 55.65 and 37.24 $m^2 g^{-1}$, respectively, calculated with a multi-point-BET method. The selected-area electron diffraction (SAED) pattern of the area displays an ambiguous halo and spot (inset of Fig. 3c), revealing that the MoO_2/N-C (500°C) is characterized by an amorphous/crystalline hybridized phase [25]. The HRTEM, fast Fourier transform (FFT) and inverse FFT (IFFT) patterns of MoO_2/N-C (350°C) (Fig. S6a, c, e) and MoO_2/N-C (700°C) (Fig. S6b, d, f) are respectively composed of bright spots and diffuse rings, indicating the variance of crystallinity when annealed at different temperatures. The results conducted from TEM and SAED hold good consistence with the XRD patterns. The IFFT patterns of the selected crystallized and amorphous areas in MoO_2/N-C (500°C) are shown in Fig. 3d, e. Clear crystal fringes can be identified and measured to be ~0.34 nm based on the line profiles inset in Fig. 3d, which is in accordance with the HRTEM results (Fig. 3c).

Sodium-ion storage properties of the as-prepared MoO_2/N-C samples were evaluated between 0.01 and 3.0 V (*vs.* Na^+/Na). The galvanostatic charge/discharge (GCD) curves of the MoO_2/N-C series are displayed and compared in Fig. S8. Impressively, MoO_2/N-C (500°C) possesses the highest capacities among the three samples, demonstrating the superior sodium-ion storage capability. The cyclic voltammetry (CV) profiles of MoO_2/N-C (500°C) at a scan rate of 0.2 mV s^{-1} are shown in Fig. 4a. In the first cathodic scan, one broad peak accompanied by two small humps are at 0.74 and 0.66 V, related to the insertion of Na^+ into MoO_2 to form Na_xMoO_2 phases and the formation of solid electrolyte interphase (SEI) film, respectively [27]. In the initial desodiation reactions, several anodic peaks are noted between 1.5 and 1.9 V, in accordance with the multistep extraction reaction of Na_xMoO_2 to MoO_2. The CV profiles of the 2nd and 3rd scans almost overlap with each other, indicating a good electrode reversibility and stability during the repeated sodium insertion and extraction. This is in accordance with the GCD curves in Fig. S8. Furthermore, rate capabilities were evaluated and the results are exhibited in Fig. 4b. The MoO_2/N-C (500°C) anode delivers the most stable and highest rate capacities among the three samples, demonstrating capacities of 238, 197, 161, 126, 80 and 67 mA h g^{-1} at current rates of 0.1, 0.2, 0.4, 1.6, 6.4 and 10 A g^{-1}, respectively. Accordingly, GCD curves at various current densities in Fig. S9 display low polarization with increased charging/discharging rates, validating good kinetics. After the current rate is switched back to 0.1 A g^{-1} again, it can restore a reversible capacity of 230 mA h g^{-1}. In contrast, both the MoO_2/N-C (350°C) and MoO_2/N-C (700°C) electrodes deliver inferior rate performances, only manifesting rate capacities of 13 and 84 mA h g^{-1} at 1.6 A g^{-1}. The Nyquist plots of the MoO_2/N-C electrodes after the first five cycles at 0.1 A g^{-1} are displayed in Fig. 4c. A semi-circle at high-frequency region and a sloping line at low frequency can be observed. MoO_2/N-C (500°C) and MoO_2/N-C (700°C) show similar charge transfer resistance (3.25 and 3.81 Ω, respectively), suggesting that the electron transport during the electrochemical Na-ion insertion/extraction is more enhanced through crystallization at a relatively high temperature. However, the diffusion behavior of sodium ions is different between MoO_2/N-C (500°C) and MoO_2/N-C (700°C). The Na-ion diffusion coefficient (D_{Na}, $cm^2 s^{-1}$) [28] can be calculated from the low-frequency area (Equation (1)).

$$D = R^2T^2 / 2A^2n^4F^4C^2\sigma_w{}^2, \quad (1)$$

where R is the universal gas constant, T is the absolute temperature, F is the Faraday constant, n is the number of electrons transferred, A is estimated as the area of the electrode and C is the concentration of Na-ions in the electrolyte [29]. According to Equation (2), σ_w is the Warburg factor and ω is the angular frequency, which is related to Z' and can be attained from the slope of the line in the low frequency area [30].

$$Z = R_e + R_{ct} + \sigma_w\omega^{-1/2}. \quad (2)$$

The D_{Na} of all the cells has been calculated based on the slope presented in Fig. 4d. The D_{Na} values of MoO_2/N-C (350°C), MoO_2/N-C (500°C) and MoO_2/N-C (700°C) are 8.7×10^{-13}, 7.3×10^{-11} and 3.9×10^{-12} $cm^2 s^{-1}$. The improved Na-ion charge transfer in MoO_2/N-C (500°C) could be

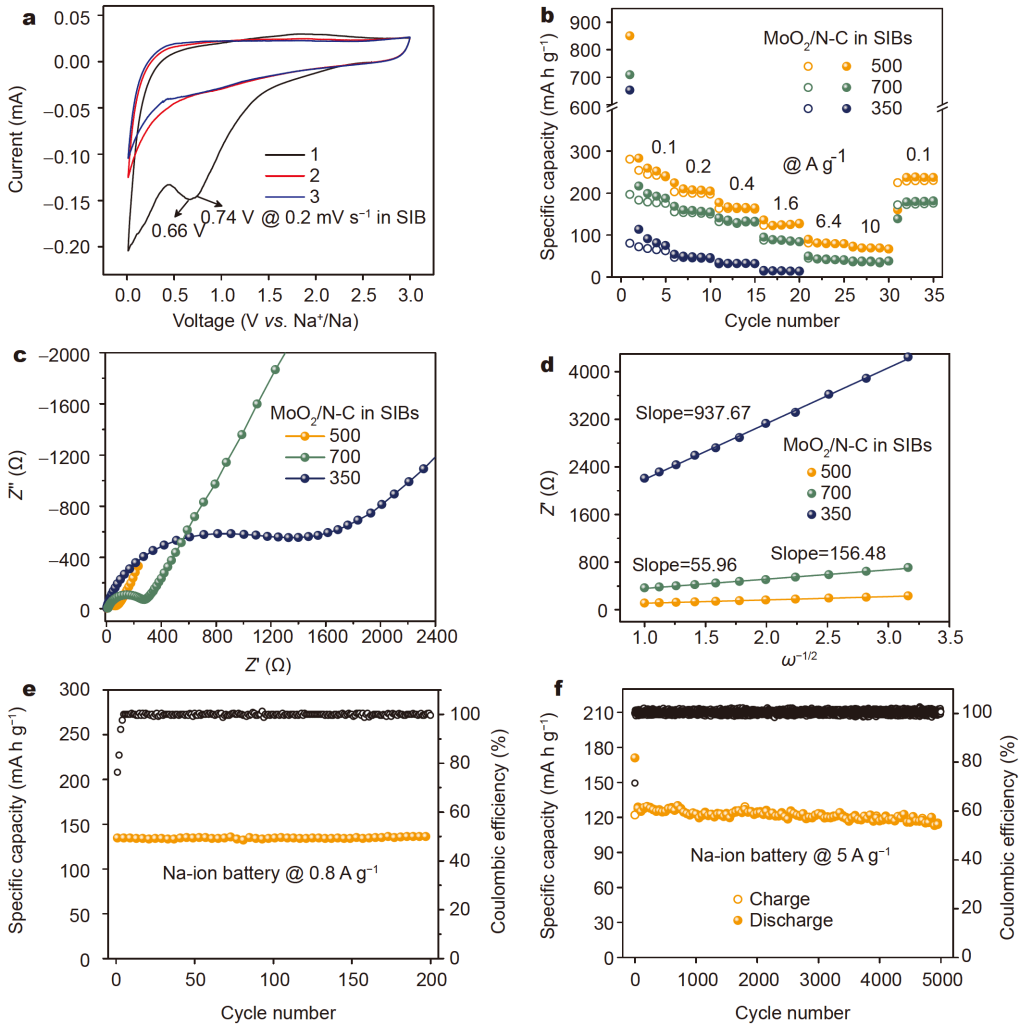

Figure 4 (a) CV curves of MoO_2/N-C (500°C) anode in SIBs at 0.2 mV s^{-1}. (b) Rate capability at various current densities in SIBs of the MoO_2/N-C series from 0.1 to 10 A g^{-1}. (c) The Nyquist plots after the first five cycles at 0.1 A g^{-1}. (d) Z' as a function of $\omega^{-1/2}$ plot in the low frequency range (the slope of fitting curves is the Warburg factor: σ_w). (e) Cycling performance of MoO_2/N-C (500°C) in SIBs at 0.8 A g^{-1} for 200 cycles. (f) Long-term cycling performance of MoO_2/N-C (500°C) in SIBs at 5 A g^{-1} for 5000 cycles.

attributed to the unique microstructure and the chemically aligned interfacial Mo–N–C bond. Cycling performance of the MoO_2/N-C (500°C) anode was tested at 0.8 and 5 A g^{-1}, as shown in Fig. 4e, f. The MoO_2/N-C (500°C) electrode manifests a high Na-ion storage capacity of 134 mA h g^{-1} with a retention rate over 98% after 200 cycles at 0.8 A g^{-1}. Even at a high current density of 5 A g^{-1}, MoO_2/N-C (500°C) can still sustain a capacity of 115 mA h g^{-1} over 5000 cycles.

The charge transfer kinetics can be further assessed by the capacitive contribution in the current response of CV curves. Fig. 5 shows the Na-ion storage behaviors of MoO_2/N-C (500°C) studied by CV measurements at different scan rates. CV curves of SIB swept from 0.2 to 1.0 mV s^{-1} display a similar contour, implying a fast charge storage mechanism (Fig. 5a). The relationship between the peak current (i) and the scan rate (v) in the CV scans could be described by Equation (3) [31]:

$$i = av^b, \quad (3)$$

where a and b are empirical constants that could be obtained by a logarithmic (log) plot of i with v, in which b=0.5 indicates a battery-type electrochemical process, while b=1.0 signifies a typical surface-controlled capacitive electrochemical process. Clearly, most b values of the cathodic and anodic peaks are identified between 0.6 and 1.0 in the MoO_2/N-C (500°C) electrode in SIBs, sug-

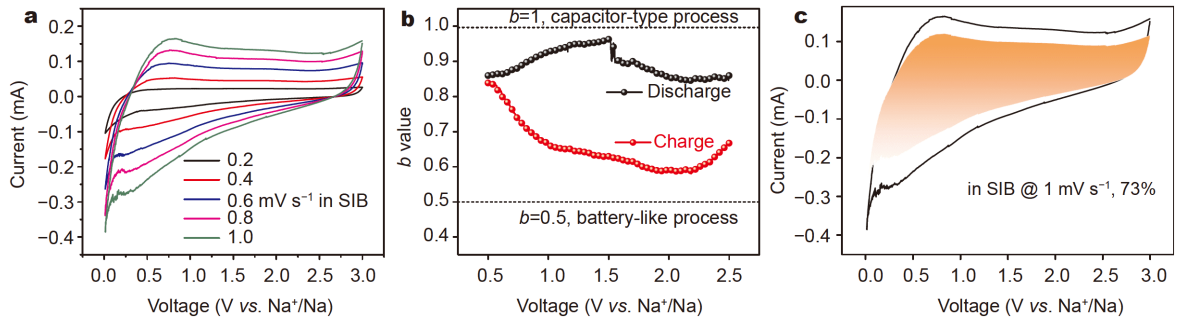

Figure 5 (a) CV curves of MoO_2/N-C (500°C) at various scan rates. (b) *b*-value distributions. (c) Capacitive contribution in the CV curves (shaded region) of SIBs at 1 mV s^{-1}.

gesting a capacitor-dominant contribution (Fig. 5b). The current response (i) at a fixed potential can be separated into capacitive process (k_1v) and diffusion-controlled reaction ($k_2v^{1/2}$). By calculating both the k_1 and k_2 constants, we can distinguish the portion of the current from surface capacitance and diffusion-controlled capacity. As illustrated in Fig. 5b, the capacitive process contributes 73% for SIBs at a sweep rate of 1.0 mV s^{-1}. The results further verify the fast kinetics nature in the Na-ion storage of MoO_2/N-C (500°C).

The outstanding Na-ion storage capability of MoO_2/N-C can be ascribed to its unique structural characteristics. First-principles DFT simulations with CASTEP were conducted to reveal the enhanced electron and ion transport properties. An N-doped graphene sheet was used as a simplified model to simulate the effects of N-doped C on the electrochemical properties during the simulation. The types of the doped-nitrogen were referred to the XPS results in Fig. 2. The optimized geometry structures of Na-ion and MoO_2 on the N-doped graphene are displayed in Fig. 6a, b, respectively. Clearly, the N-doping, particularly in form of our present N-doped form, pyridinic-N, can considerably increase the affinity of carbon to both Na and MoO_2, leading to high adsorption energies (E_{ads}) of −3.07 eV (Na) and −9.56 eV (MoO_2). The high affinity towards Na-ion can facilitate the concentration of Na-ions on the surface of the N-doped carbon, so that more Na-ions can be supplied to subsequent electrochemical reaction. The formation of interfacial Mo–N chemical bond is displayed in Fig. 6c, which is in consistent with the XPS result. The charge separation of the MoO_2/N-C heterostructures is revealed by the calculated charge density differences. As seen from Fig. 6c, charge redistributions mainly occur at the interfacial region. The accumulated charge at the interface suggests an improved charge transfer [32] within MoO_2 and the N-doped carbon through Mo–N–C interfacial chemical bond, which is expected to enhance the rate performance of the electrode material during the charge/discharge process [31].

To further estimate the fast kinetics in electrochemical Na-ion storage, a hybrid Na-ion capacitor (SIC) was as-

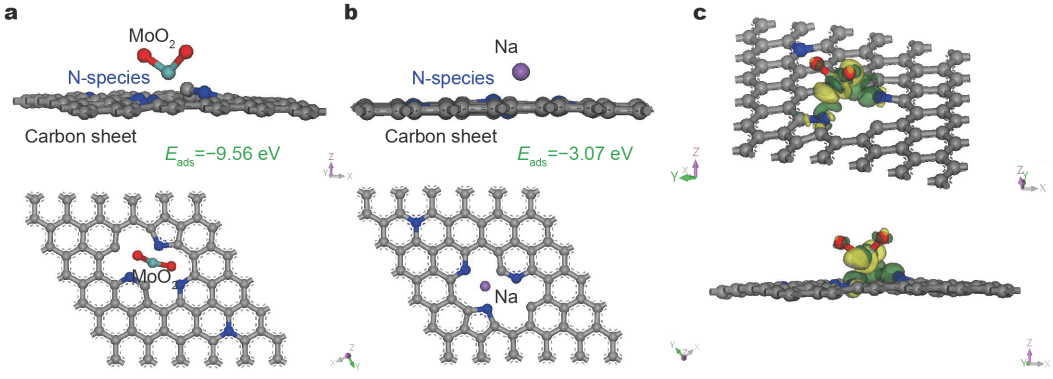

Figure 6 Optimized geometry configurations of (a) MoO_2 and (b) Na-ion on the N-doped graphene surface, together with the corresponding adsorption energies (E_{ads}). (c) The charge difference of top view and side view of the charge density difference of MoO_2/N-C. The yellow/green cloud represents the negative/positive charge differences, respectively.

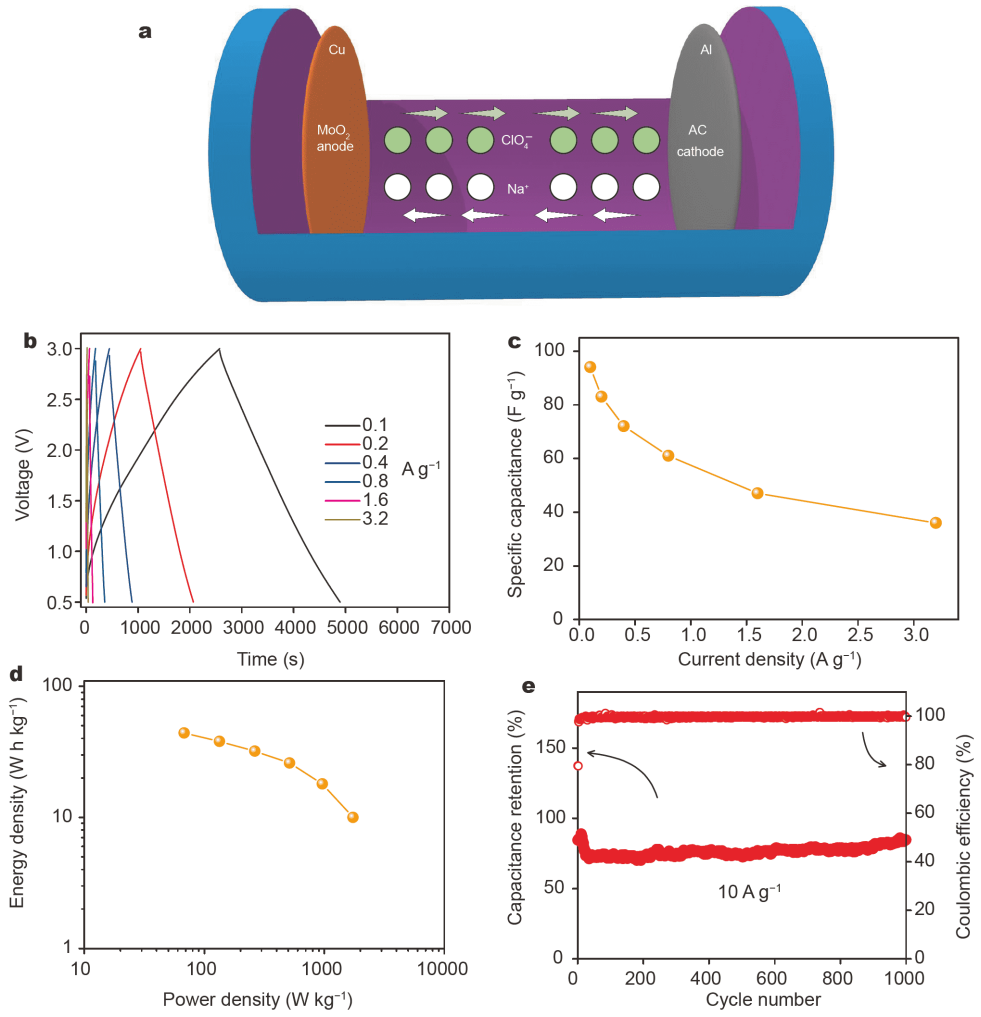

Figure 7 (a) Schematic illustration of the charge-storage mechanism for the as-assembled SIC. (b) Profile of the charge/discharge curves of SIC. (c) Specific capacitances at various current densities and (d) Ragone plot of the as-prepared SIC. (e) Cycle performance of SIC at 10 A g^{-1}.

sembled with purchased activated carbon (AC, specific surface area: ~1700 m^2 g^{-1}) [31] as the counter electrode. Fig. 7a illustrates the charge-storage mechanism for the as-assembled SIC. During the charge storage process, the Na-ions could contact MoO_2/N-C through a Faradaic reaction and a predominant pseudocapacitive process. Meanwhile, the perchlorate anions can be adsorbed on the porous surface or defect sites of the AC cathode. Fig. 7b exhibits the GCD curves at current densities from 0.1 to 3.2 A g^{-1}. The voltage profiles at all these current densities show a semi-triangle shape, indicative of a combination of charge storage mechanisms based on Faradaic and non-Faradaic reactions [33]. On the basis of the GCD results, the specific capacitance (Fig. 7c), energy densities and power outputs (Fig. 7d) of the as-assembled SIC can be calculated based on the total mass of both the cathode and the anode active materials. As can be seen in Fig. 7d, for example, the SIC can exhibit an energy density of 15 W h kg^{-1} at a power output of 1760 W kg^{-1}. The SIC also shows outstanding cycling stability at a high current density of 10 A g^{-1}, exhibiting a capacitance retention of 92.4% after 1000 cycles, with the coulombic efficiencies approaching 100% (Fig. 7e).

CONCLUSIONS

We employed a facile topochemical transformation to synthesize MoO_2/N-C with interfacial Mo–N chemical bond. The formation of MoO_2 *via* phase segregation, together with the carbonization of polydopamine precursor is believed to effectively reduce the undesired grain

growth and help to form a porous nanostructure. Chemically bridged MoO_2 with N-doped carbon substrate facilitates fast charge transfer. When evaluated in a Na-ion half-cell configuration, the hybrid triggers an obvious synergetic effect of both materials, resulting in superior Na-ion storage performance in terms of excellent rate capability and outstanding cycling stability. The enhanced chemical affinities of the N-doped carbon to Na-ions and MoO_2 are further elucidated by first-principles DFT calculations. Owing to this unique microstructure and the chemical bonding at heterointerface, the MoO_2/N-C also shows good performance in SIC. This work provides an effective strategy to design TMOs heterojunctioned with carbon for high-performance energy storage beyond LIBs. It also highlights the efficient interfacial coupling for further improving the overall electrochemical performance of the composite-electrode materials.

Received 10 March 2020; accepted 23 April 2020; published online 28 June 2020

1 Massé RC, Uchaker E, Cao G, *et al.* Beyond Li-ion: electrode materials for sodium- and magnesium-ion batteries. Sci China Mater, 2015, 58: 715–766
2 Huang H, Cui J, Liu G, *et al.* Carbon-coated $MoSe_2$/MXene hybrid nanosheets for superior potassium storage. ACS Nano, 2019, 13: 3448–3456
3 Fan L, Li X. Recent advances in effective protection of sodium metal anode. Nano Energy, 2018, 53: 630–642
4 Shadike Z, Zhao E, Zhou YN, *et al.* Advanced characterization techniques for sodium-ion battery studies. Adv Energy Mater, 2018, 8: 1702588
5 Liu X, Hao Y, Shu J, *et al.* Nitrogen/sulfur dual-doping of reduced graphene oxide harvesting hollow $ZnSnS_3$ nano-microcubes with superior sodium storage. Nano Energy, 2019, 57: 414–423
6 Jian Z, Luo W, Ji X. Carbon electrodes for K-ion batteries. J Am Chem Soc, 2015, 137: 11566–11569
7 Wei Z, Wang D, Li M, *et al.* Fabrication of hierarchical potassium titanium phosphate spheroids: a host material for sodium-ion and potassium-ion storage. Adv Energy Mater, 2018, 8: 1801102
8 Chen Z, Yin D, Zhang M. Sandwich-like MoS_2@SnO_2@C with high capacity and stability for sodium/potassium ion batteries. Small, 2018, 14: 1703818
9 Mao M, Yan F, Cui C, *et al.* Pipe-wire TiO_2-Sn@carbon nanofibers paper anodes for lithium and sodium ion batteries. Nano Lett, 2017, 17: 3830–3836
10 Hu S, Yin F, Uchaker E, *et al.* Facile and green preparation for the formation of MoO_2-GO composites as anode material for lithium-ion batteries. J Phys Chem C, 2014, 118: 24890–24897
11 Zhao X, Wang HE, Chen X, *et al.* Tubular MoO_2 organized by 2D assemblies for fast and durable alkali-ion storage. Energy Storage Mater, 2018, 11: 161–169
12 Zhao X, Wang HE, Cao J, *et al.* Amorphous/crystalline hybrid MoO_2 nanosheets for high-energy lithium-ion capacitors. Chem Commun, 2017, 53: 10723–10726
13 Hao J, Zhang J, Xia G, *et al.* Heterostructure manipulation *via in situ* localized phase transformation for high-rate and highly durable lithium ion storage. ACS Nano, 2018, 12: 10430–10438
14 Yang JL, Zhao SX, Lu YM, *et al.* *In-situ* topochemical nitridation derivative MoO_2-Mo_2N binary nanobelts as multifunctional interlayer for fast-kinetic Li-sulfur batteries. Nano Energy, 2020, 68: 104356
15 Miao ZH, Wang PP, Xiao YC, *et al.* Dopamine-induced formation of ultrasmall few-layer MoS_2 homogeneously embedded in N-doped carbon framework for enhanced lithium-ion storage. ACS Appl Mater Interfaces, 2016, 8: 33741–33748
16 Yang N, Cheng H, Liu X, *et al.* Amorphous/crystalline heterophase Pd nanosheets: one-pot synthesis and highly selective hydrogenation reaction. Adv Mater, 2018, 30: 1803234
17 Ma FX, Wu HB, Xia BY, *et al.* Hierarchical β-Mo_2C nanotubes organized by ultrathin nanosheets as a highly efficient electrocatalyst for hydrogen production. Angew Chem Int Ed, 2015, 54: 15395–15399
18 Xia C, Zhou Y, Velusamy DB, *et al.* Anomalous Li storage capability in atomically thin two-dimensional sheets of nonlayered MoO_2. Nano Lett, 2018, 18: 1506–1515
19 Su D, Zhang X, Wu A, *et al.* CoO-Mo_2N hollow heterostructure for high-efficiency electrocatalytic hydrogen evolution reaction. NPG Asia Mater, 2019, 11: 78
20 Zhao X, Wang HE, Massé RC, *et al.* Design of coherent anode materials with 0D Ni_3S_2 nanoparticles self-assembled on 3D interconnected carbon networks for fast and reversible sodium storage. J Mater Chem A, 2017, 5: 7394–7402
21 Li X, Guo G, Qin N, *et al.* SnS_2/TiO_2 nanohybrids chemically bonded on nitrogen-doped graphene for lithium-sulfur batteries: synergy of vacancy defects and heterostructures. Nanoscale, 2018, 10: 15505–15512
22 Tang YJ, Wang Y, Wang XL, *et al.* Molybdenum disulfide/nitrogen-doped reduced graphene oxide nanocomposite with enlarged interlayer spacing for electrocatalytic hydrogen evolution. Adv Energy Mater, 2016, 6: 1600116
23 Huang S, Li Z, Wang B, *et al.* N-doping and defective nanographitic domain coupled hard carbon nanoshells for high performance lithium/sodium storage. Adv Funct Mater, 2018, 28: 1706294
24 Zhao X, Gong F, Zhao Y, *et al.* Encapsulating NiS nanocrystal into nitrogen-doped carbon framework for high performance sodium/potassium-ion storage. Chem Eng J, 2020, 392: 123675
25 Zhao D, Qin J, Zheng L, *et al.* Amorphous vanadium oxide/molybdenum oxide hybrid with three-dimensional ordered hierarchically porous structure as a high-performance Li-ion battery anode. Chem Mater, 2016, 28: 4180–4190
26 Zhao X, Zhao Y, Huang B, *et al.* Dual interface coupled molybdenum diselenide for high-performance sodium ion batteries and capacitors. J Power Sources, 2020, 446: 227298
27 Zhao C, Yu C, Zhang M, *et al.* Ultrafine MoO_2-carbon microstructures enable ultralong-life power-type sodium ion storage by enhanced pseudocapacitance. Adv Energy Mater, 2017, 7: 1602880
28 Zhu M, Luo Z, Pan A, *et al.* N-doped one-dimensional carbonaceous backbones supported $MoSe_2$ nanosheets as superior electrodes for energy storage and conversion. Chem Eng J, 2018, 334: 2190–2200
29 Liu C, Zhang C, Fu H, *et al.* Exploiting high-performance anode through tuning the character of chemical bonds for Li-ion batteries and capacitors. Adv Energy Mater, 2017, 7: 1601127
30 Shen Q, Jiang P, He H, *et al.* Encapsulation of $MoSe_2$ in carbon fibers as anodes for potassium ion batteries and nonaqueous bat-

tery-supercapacitor hybrid devices. Nanoscale, 2019, 11: 13511–13520
31 Zhao X, Cai W, Yang Y, *et al.* $MoSe_2$ nanosheets perpendicularly grown on graphene with Mo–C bonding for sodium-ion capacitors. Nano Energy, 2018, 47: 224–234
32 Zhang F, Shen Y, Shao M, *et al.* $SnSe_2$ nanoparticles chemically embedded in a carbon shell for high-rate sodium-ion storage. ACS Appl Mater Interfaces, 2019, 12: 2346–2353
33 Wang H, Zhu C, Chao D, *et al.* Nonaqueous hybrid lithium-ion and sodium-ion capacitors. Adv Mater, 2017, 29: 1702093

Acknowledgements This work was supported by the National Natural Science Foundation of China (51804089) and the Guangxi Key Laboratory of Electrochemical and Magneto-chemical Functional Materials (EMFM20181114). Zhao X thanks the support of the research starting foundation of CAEP (PY20200038).

Author contributions Huang B and Zhao X designed and prepared the samples; Liu S, Li Y, Yang J, Chen Q, Xiao S and Zhang W performed the characterizations and data analysis; Wang HE finished the first-principles calculation; Huang B and Zhao X wrote the paper with support from Cao G; Cao G contributed to the theoretical analysis. All authors contributed to the general discussion.

Conflict of interest The authors declare that they have no conflict of interest.

Supplementary information Supporting data are available in the online version of the paper.

Bin Huang received his BSc degree (2009) and MSc degree (2012) from the College of Chemistry and Chemical Engineering, Central South University, and received his PhD degree (2016) from the School of Metallurgy and Environment, Central South University. In January 2017, he joined the College of Chemistry and Bioengineering, Guilin University of Technology. His current research focuses on the processing and modification of electrode materials for lithium- & sodium-ion batteries.

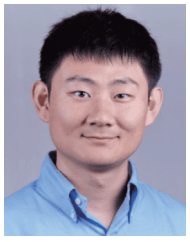

Xu Zhao is currently an assistant professor of the Department of Energetic Materials at the Institute of Chemical Materials, China Academy of Engineering Physics (ICM, CAEP). He obtained his PhD degree from Harbin Institute of Technology in 2019. From 2015 to 2017, he was a visiting scholar in Prof. Guozhong Cao's group at the Materials Science and Engineering, University of Washington. His current research focuses on the design of high-performance energetic materials and advanced electrodes for electrochemical energy storage devices.

Hong-En Wang received his PhD degree from the City University of Hong Kong (2012). Then he worked as an associate professor at Wuhan University of Technology (2012–2019). He joined the College of Physics and Electronics Information of Yunnan Normal University in 2020. His current research interests mainly focus on photovoltaic materials, nanostructured electrode materials for Li/Na-ion and Li-S batteries, etc.

Guozhong Cao is Boeing-Steiner professor of Materials Science and Engineering, professor of Chemical Engineering and adjunct professor of Mechanical Engineering at the University of Washington, Seattle, WA. He is one of the Thomson Reuters Highly Cited Researchers with a total citation of 42,000 and an h-index of 102. His current research focuses on the chemical processing of nanomaterials for solar cells, batteries, and supercapacitors as well as actuators and sensors.

通过构筑界面Mo–N–C键提高MoO_2/氮掺杂碳复合材料的钠离子存储性能

黄斌[1], 刘爽[1], 赵煦[2*], 李延伟[1], 杨建文[1], 陈权启[1], 肖顺华[1], 张文华[2], 王洪恩[4*], 曹国忠[3*]

摘要 钠离子电池因具有与锂离子电池接近的工作电压且具有丰富的钠资源优势而受到广泛关注, 并有望成为商业化锂离子电池的替代产品. 然而, 开发合适的钠离子电池负极材料仍存在一些挑战. 本文通过一种简单有效的碳化诱导拓扑化学转化法合成了一种MoO_2/氮掺杂碳复合材料(MoO_2/N-C), 其中MoO_2纳米晶嵌入在氮掺杂的碳基质里, 并与之形成Mo–N–C键. 用该MoO_2/N-C复合材料组装的钠离子半电池具有很好的倍率性能和循环稳定性, 可在5 A g^{-1}的电流密度下循环超5000周. 物理化学表征和基于密度泛函理论的第一性原理计算表明, MoO_2和氮掺杂碳界面上的化学键合对复合材料电化学性能的提高起了重要作用. 更重要的是, 该化学键合可有效促进界面上的电荷转移. 基于此, 用该复合材料和活化碳组装的钠离子电容器在1760 W kg^{-1}功率密度下可提供15 W h kg^{-1}的能量密度, 同时在10 A g^{-1}的电流密度下循环1000周后具有92.4%的电容保持率. 本文介绍的界面化学键的构筑有望为面向储能器件的高性能电极的设计提供参考.

